Mancini, Federica; Remes, Heikki; Romanoff, Jani; Gallo, Pasquale

Influence of weld rigidity on the non-linear structural response of beams with a curved distortion

Published in:
Engineering Structures

DOI:
10.1016/j.engstruct.2021.113044

Published: 01/11/2021

Document Version
Publisher's PDF, also known as Version of record

Engineering Structures 246 (2021) 113044

Contents lists available at ScienceDirect

Engineering Structures

journal homepage: www.elsevier.com/locate/engstruct

Influence of weld rigidity on the non-linear structural response of beams with a curved distortion

Federica Mancini *, Heikki Remes, Jani Romanoff, Pasquale Gallo

Department of Mechanical Engineering, Aalto University, Otakaari 4, Espoo, 02150, Finland

ARTICLE INFO

Keywords:
Non-linear beam theory
Thin plate
Angular misalignment
Welded joint
Weld rigidity
Fixity factor
Rotational spring
Structural stress
Hot-spot
Stress magnification factor

ABSTRACT

This study investigates an analytical beam model to improve the analyses of welded thin plates with welding-induced curved distortions. The model addresses the rigidity of a butt-welded joint and its effect on plate bending and structural stress by including a rotational spring at the welded end. The spring rotational stiffness, k_a, is replaced by the fixity factor, ρ_a. The validity of the model is based on the assumption of small displacement and moderate rotation of the mid-plane of the welded plate. Using the Finite Element Analysis of a two-dimensional model, a semi-analytical method for the fixity factor computation is developed. Compared with the numerical analysis, the beam model showed a maximum error of 3% in deflection and hot-spot structural stress. Results suggest that the fixity factor is mainly dependent on the width of the weld bead and the far-end constraint. The introduction of ρ_a can improve the analytical solution by 9% in the evaluation of the hot-spot structural stress. Neglecting the non-ideal joint rigidity may lead up to 54% underestimation in terms of fatigue life, when the S–N curve slope, m, equals 5. However, the relevance of ρ_a decreases for increasing geometric slenderness of the welded plates.

1. Introduction

Lightweight design is essential in different engineering fields where structural optimisation aims at reduced economic and environmental impact, whilst enhancing the technical performance [1].

Thin-walled structures made of high-strength steel are an attractive solution to achieve the lightweight design in the shipbuilding industry, where the use of steel is well-established in the manufacturing process. However, the thickness reduction causes higher susceptibility to welding-induced distortions, which lead to a geometric non-linear response under axial loading. Research in the field of marine structures pointed out that the geometric non-linearity is a major source of uncertainty in the fatigue assessment of structural components [2–5]. For an efficient and flexible routine at the early design stages, the current recommendations for the fatigue assessment of welded components provide analytical solutions based on the nominal or structural hot-spot stress approach [6,7]. For butt-welded plates, the latter evaluates the structural stress at the weld (i.e., the hot-spot) as the nominal stress, σ_N, multiplied by a stress magnification factor, k_m. The nominal stress must satisfy the global equilibrium conditions, while the stress magnification factor encompasses the local stress concentration caused by the initial distortion. The current solutions for the k_m factor account only for a flat distortion, i.e. for a global angular misalignment that is constant between plate supports [8]. This simplification limits the validity of the solutions to plate thicknesses, t, of at least 5 mm [5,9]. On the other hand, the mechanics of welded thin-plates with curved distortion is not fully understood, yet. Thereby, the lack of a proper analytical solution has made the Finite Element Analysis (FEA) the only computational approach for the design of these lightweight solutions. Moreover, for large structures like passenger ships, a time-consuming FEA is highly inefficient in the early stages of the design process. For these reasons, the shipbuilding design standards are still preventing the use of *thin* plates, i.e. plates with $t \leq 5$ mm [10]. Although the need for improved analytical models emerged especially in the shipbuilding field, the study concerns any application of thin-plate butt-welded joints with a curved initial distortion.

In order to analyse the effect of a welding-induced curved distortion, several studies have proposed improved solutions focusing on an angular misalignment with a local variation; see [11–16]. These solutions simplify the curved distortion as shown in Fig. 1. In the figure, the curvature on the welded plates induces a local angle, α_L, at the weld fusion-line, superimposed to the global angle, α_G, of the flat distortion. It should be noted that the plates have equal length l and thickness t. The studies consider a linear-elastic, one-dimensional (1D) beam idealisation of the structural problem. In fact, thin and slender (i.e. $l/t > 20$) isotropic plates generally show negligible out-of-plane

* Corresponding author.
E-mail address: federica.mancini@aalto.fi (F. Mancini).

https://doi.org/10.1016/j.engstruct.2021.113044
Received 2 April 2021; Received in revised form 28 July 2021; Accepted 13 August 2021
Available online 31 August 2021

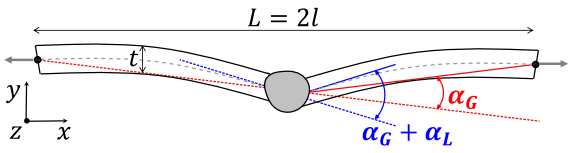

Fig. 1. Definition of global, α_G, and local, α_L, angular misalignment in a simplified welding-induced curved distortion on butt-welded thin plates of equal length l and thickness t.

normal and shear stresses (i.e., σ_y and τ_{xy} over the plate thickness, respectively). Moreover, the transverse in-plane shear stress (i.e., τ_{xz}) has negligible contribution in terms of deflections for plates with an aspect ratio larger than 10 (i.e. plate strips) [17,18]. Thereby, the beam well-approximates deflections over the main axis of a thin plate strip, which also neglects any initial distortion in the transverse direction.

A further improvement is proposed by Mancini et al. [16], where the beam analysis is extended to non-ideal rotational constraints at the beam ends (a and b). The study models rotational constraints (or boundary conditions, BCs) through rotational springs with stiffness $k_{a,b}$. Since the stiffness varies between 0 and ∞ (i.e., ideally pinned to fixed rotation, respectively), it is conventionally substituted by fixity factors, $\rho_{a,b}$ [19–21]. The use of fixity factors is usually found in the stability analysis of columns in frames. The role played by these terms is to account for the interaction of an isolated member with the neighbouring structure, which modifies its actual rotational stiffness [21]. In the present analysis, the interacting members are the beam and the joint itself. The end b is ideally constrained, as the variation of ρ_b shows a minor impact on the k_m factor, if compared with the constraint at weld location [16]. Instead, a fictitious spring is located at the weld fusion-line, which becomes the origin of the beam model, namely a. The spring can only weaken the rotational constraint at the beam origin if compared to the ideally clamped condition. In terms of the fixity factor, the interesting range remains within 0 (i.e., pinned condition) and 1 (i.e., clamped condition). A fixity factor approaching 0 would suggest that the deformation of the weld area dissipates the majority of the bending action, reducing the moment reaction needed at the left edge of the welded plate. On the contrary, a more rigid weld has a higher moment capacity, thus conveying the moment reaction to the left edge of the plate with minimum deformation of the welded area.

This paper further develops the previous research [16] by proposing a semi-analytical method for the computation of the fixity factor at the welded end of a thin plate strip under uniaxial tensile load. The fixity factor is computed by FEA of a two-dimensional (2D) thin plate model, including the weld shape. The FEA provides the nodal slope of the mid-plane at the weld fusion-line (i.e. the boundary between the welded region and the plate). This slope is equalled to its analytical expression to evaluate ρ_a. The analytical model is validated in terms of mid-plane deflection and structural hot-spot stress by comparison against the numerical solution. The numerical hot-spot stress is provided by the structural stress approaches of through-thickness linearisation and surface stress quadratic extrapolation to the hot-spot, as recommended in [7]; see Section 2.2.1. Additionally, a sensitivity analysis shows the impact of different weld and plate geometries, load levels, and far-end constraints on the fixity factor ρ_a. Finally, the validity of the results is studied for different geometric slenderness ratios.

2. Methodology

2.1. Analytical model

The 1D beam model in Fig. 2 represents the longitudinal (and main) direction of one of the two butt-welded plates. In the figure, the left-end a of the beam corresponds to the weld fusion-line, while the right end b is loaded by a tensile force, P. As only half of the welded structure of

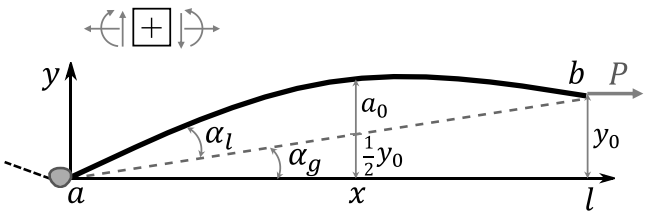

Fig. 2. Beam model with an initial curved distortion described by a linear lateral sway superimposed to a half-sine curvature. A tensile load, P, is applied at the right end, b (or far-end with respect to the weld location a).

Fig. 1 is modelled, the angles are defined based on the baseline (i.e., the beam without any distortion) as a reference. Consequently, the angles are indicated with lowercase subscripts. When the welded structure is fully symmetric with respect to the weld line, $\alpha_l = \alpha_L/2$ and $\alpha_g = \alpha_G/2$. The distorted shape $w_0(x)$ over the beam length l is simplified to a superposition of a linear lateral sway $w_{0,y_0}(x)$ and a half-sine curvature $w_{0,a_0}(x)$ of maximum amplitudes y_0 and a_0, respectively (see Eq. (1)).

$$w_0(x) = w_{0,y_0}(x) + w_{0,a_0}(x) = \frac{y_0 x}{l} + a_0 \sin\left(\frac{\pi x}{l}\right), \tag{1}$$

The analytical model follows the Bernoulli–Navier hypotheses [17] and uses the von-Kármán axial strain definition. The latter accounts for secondary bending effects and applies to a kinematic of small displacements and moderate rotations (commonly, up to 10 deg). The strain is defined as [18]:

$$\varepsilon_x = \left[\frac{du}{dx} + \frac{1}{2}\left(\frac{dw}{dx}\right)^2\right] - z\frac{d^2w}{dx^2}. \tag{2}$$

The differential equations related to the beam axial displacement, δu, and deflection, δw, are derived according to the Hooke's Law for linear-elastic materials (i.e., the normal stress is $\sigma_x = E\varepsilon_x$, whit E Young's modulus of the material) and the principle of virtual displacement; see Eq. (3) [22], where N and M are the internal axial force and bending moment, respectively.

$$\begin{cases} \delta u: & -\dfrac{dN}{dx} = 0 \\ \delta w: & -\dfrac{d}{dx}\left(\dfrac{dw}{dx}N\right) - \dfrac{d^2M}{dx^2} = 0 \end{cases} \tag{3}$$

In Eq. (3), the bending moment can be approximated by Eq. (4), where the superscript (′) indicates a derivative with respect to x, and r is the radius of curvature of the deflected beam. In the equation, EI_{xx} is the flexural stiffness of the beam, where I_{xx} is the second moment of inertia. The approximation $1/r \sim w''$ is commonly accepted in the case of moderate rotations and results in 1% error if w' does not exceed 0.08, i.e. is less than 5 deg [17].

$$M(x) = -\frac{EI_{xx}}{r} \approx -EI_{xx}w''(x) \tag{4}$$

Considering Eq. (4), the ordinary differential equation (ODE) in terms of beam deflection is obtained by integrating twice the second expression in Eq. (3), substituting $w(x)$ with $w(x) + w_0(x)$, and applying the problem boundary conditions. For simplicity, it is possible to apply the principle of linear superposition to treat the flat and curved distortions separately. Then, the two ODEs for the beam model with half-sine curvature and the beam with linear lateral sway are, respectively:

$$w_1''(x) - k^2 w_1(x) = +k^2 a_0 \sin\left(\frac{\pi x}{l}\right), \tag{5}$$

$$w_2''(x) - k^2 w_2(x) = -\frac{M_a}{EI_{xx}} + \frac{M_a + M_b - P(Y - y_0)}{EI_{xx}l}x. \tag{6}$$

In the equations, $k = \sqrt{(P/EI_{xx})}$, M_a and M_b are the bending moments at the beam ends, while Y is the final vertical position of the far-end b of the beam. The derivation of a closed-form solution of the

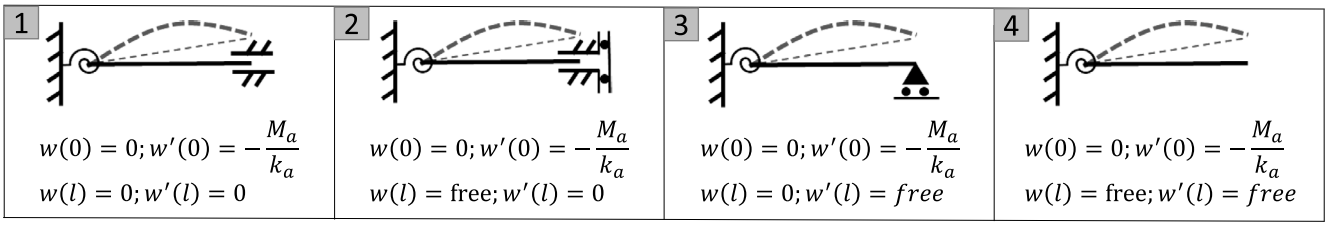

Fig. 3. Deflection $w(x)$ and slope-deflection $w'(x)$ boundary condition configurations for the beam model of length l with a rotational spring of stiffness k_a at the left end (i.e., at $x = 0$).

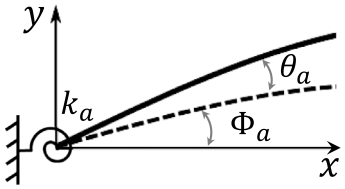

Fig. 4. Definition of the beam rotation angle Φ_a and the spring rotation angle θ_a at the left end, a, of the beam.

ODEs first needs the deflection BCs. Consequently, the deflection equations $w_1(x)$ and $w_2(x)$ (and their derivatives) are linearly superimposed, i.e., $w(x) = w_1(x)+w_2(x)$, where $w(x)$ becomes the total deflection of the curved beam. As the flat and curved beams are first analysed separately, the possible deflection BCs (i.e. $w(0)$ and $w(l)$) in the actual structural problem can be considered only once. In this case, the half-sine curved beam is always fixed at both ends, i.e. $w_1(0) = w_1(l) = 0$. Instead, the deflection of the beam with linear lateral sway is 0 at weld location, while it can be either free or fixed at the far-end (i.e., $w_2(l) = [0, Y-y_0]$, as for the actual structure). Finally, the slope-deflection BCs are applied on the total slope $w'(x) = w'_1(x) + w'_2(x)$. The BC at the welded end is determined by the action of the rotational spring, while the far-end rotation is either zero or free. Combining these total deflection and slop-deflection BCs, all the possible deformation mechanisms of the structural system of interest are covered. This study considers all these combinations, which are summarised in Fig. 3.

In Fig. 3, the term k_a represents the rotational stiffness of the spring at the welded beam end. In the analytical derivation, k_a is included in terms of the fixity factor ρ_a. The relation between the two terms is based on two definitions. First:

$$k_a = -\frac{M_a}{\theta_a}, \tag{7}$$

where θ_a is the spring rotation. The stiffness is positive when the moment counteracts the end rotation (i.e., when they have opposite direction). Second:

$$\rho_a = \frac{\Phi_a}{\Phi_a + \theta_a}, \tag{8}$$

where Φ_a is the slope depending on the beam flexural stiffness and its BCs at both ends; see Fig. 4.

For a generalised formulation of the slope at the welded end, it is useful to consider the analysis of a straight, ideal, simply supported beam subjected to external end moments M_a and M_b (if $M_b \neq 0$). These moments correspond to the internal moment reactions derived for the beam in Fig. 2. As shown by Hellesland [21], if the slope BCs are solved for M_a,

$$M_a = \frac{EI_{xx}}{l}\Phi_a\left[4\left(1 + 0.5\frac{\Phi_b}{\Phi_a}\right)\right]. \tag{9}$$

In Eq. (9), the term in square brackets can be substituted by a new term b^*. The latter becomes very useful in the case of non-ideal rotational constraints. In fact, by substituting the ratio Φ_b/Φ_a by the actual slope ratio, it is possible to use the term b^* as a correction to the ideal flexural stiffness of the beam. In this study, $\Phi_b/\Phi_a = \Phi_b/(\Phi_a+\theta_a)$. Accordingly, $b^*_{(1)(2)} = 4$, and $b^*_{(3)(4)} = 3$, with subscripts referring to BC configurations of Fig. 3. According to the above equations,

$$\rho_a = \frac{\Phi_a}{\Phi_a + \theta_a} = \frac{1}{1 + \frac{\theta_a}{\Phi_a}} = \frac{1}{1 + \frac{-M_a}{k_a}\frac{b^* EI_{xx}}{M_a l}} = \frac{1}{1 - \frac{b^* EI_{xx}}{k_a l}}. \tag{10}$$

Finally, the rotational stiffness of the spring can be substituted in the slope BCs in Fig. 3 as:

$$k_a = \frac{b^*}{\frac{1}{\rho_a} - 1}\frac{EI_{xx}}{l}. \tag{11}$$

Notice that these definitions are used with consistency with the right-hand rule for both the numerical and analytical models. When the beam kinematics is solved, the hot-spot structural stress can be defined as in Eq. (12), where σ_m and σ_b are the membrane and bending moment, respectively, and $I_{xx} = b_p t^3/12$.

$$\sigma_{HS} = \sigma_m + \sigma_b(0)|_{y=t/2} = \frac{P}{b_p t} + \frac{M_a}{I_{xx}}\frac{t}{2} \tag{12}$$

Consequently, the stress magnification factor is defined as:

$$k_m = \frac{\sigma_{HS}}{\sigma_m} = 1 + \frac{6M_a}{Pt}. \tag{13}$$

The final formulations for the k_m factor with and without non-ideal rotational constraint at the welded end are shown in Appendix A. In this study, $\sigma_m = \sigma_N$, since uniaxial load is considered.

2.2. Finite element analysis

In this study, the FEA provides the slope at the weld fusion-line, which is needed for the computation of the fixity factors for selected geometries of the welded joint. Furthermore, the FEA is utilised to calculate a reference solution in order to study the mechanics of the welded thin plates with initial curvature.

2.2.1. The finite element (FE) structural stress approaches

The reference solution in terms of structural stress is assessed according to fatigue design recommendations for welded plates [7]. The commonly accepted approaches are the through-thickness linearisation (TTL), the surface stress linear or quadratic extrapolation to the hot-spot (LE or QE), the Haibach's approach and Yamada's method. These approaches allow for the determination of the hot-spot stress in the presence of local effects due to the notch area. This study applies the TTL at the hot-spot location and the QE approach in the validation of the analytical model, as they are shown to be suitable methods for thin plates; see e.g. [23].

According to the TTL approach, the local non-linear stress distribution near the weld toe must be equilibrium-equivalent to a linear stress distribution away from the weld [24]. In the case of 2D thin plate models, the linearisation will only depend on the normal stress (see Eq. (14), where $A = b_p t$ and $W = y/I_{xx}$, with t and y defined in Fig. 5(a), and b_p representing the plate width), thus dropping the shear effect contribution introduced by Dong et al. [24]; see, for instance, [23,25].

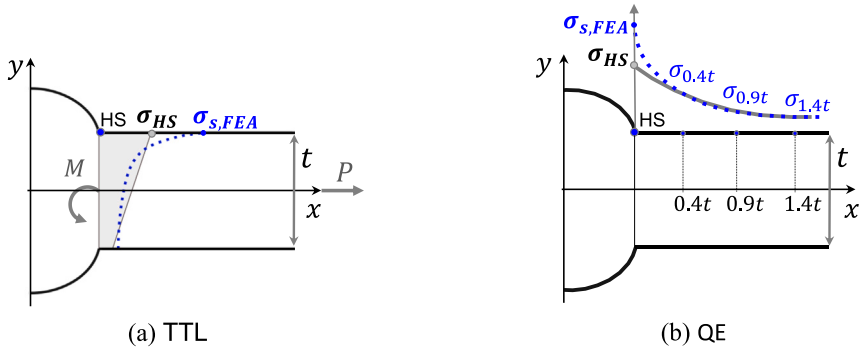

Fig. 5. Representation of (a) Through-Thickness Linearisation (TTL) and (b) Quadratic Extrapolation to the hotspot (QE) for the structural stress assessment.

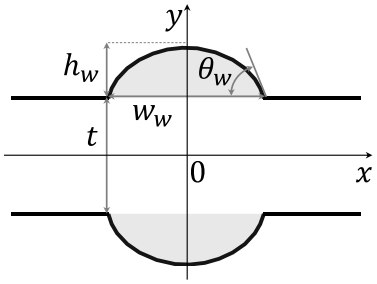

Fig. 6. Geometric dimensions of an ideally symmetric butt welded joint.

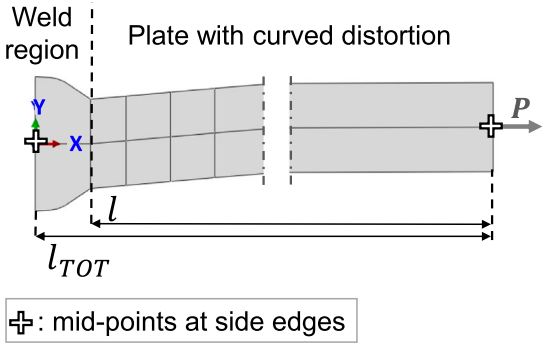

Fig. 7. FE model profile sketch of weld region and distorted plate. The mid-points at side edge surfaces are shown.

In this paper, the stress is linearised through trapezoidal integration in Eq. (15), where $f(y)$ is a general function of y and N is the number of nodes over the thickness. The TTL approach is usually preferred, being the most physically correct among the structural stress approaches.

$$\sigma_s = \frac{P}{A} + \frac{M}{W} \rightarrow \sigma_s = \frac{l}{t}\int_0^t \sigma(y)dy + \frac{6}{t^2}\int_0^t \sigma(y)\left(\frac{t}{2} - 1\right)dy \tag{14}$$

$$\int_0^t f(y)dy = \frac{t}{2N}\left[f(y_0) + 2f(y_1) + \cdots + 2f(y_{N-1}) + f(y_N)\right] \tag{15}$$

The method of surface stress extrapolation to the hot-spot was initially developed for thick tubular joints. Since the local stress concentration typically affected the stress distribution up to $(0.3, 0.4) \cdot t$ away from the weld location (i.e. the hot-spot), reference points for a linear extrapolation approach were selected accordingly. Based on the same observations, the QE approach refers to points at $(0.4, 0.9, 1.4) \cdot t$; see Eq. (16). Here, the quadratic solution is preferred to the linear one because of the steeper stress gradients expected in thin plates with local angular misalignment; see Fig. 5(b).

$$\sigma_{HS} = 2.52\sigma_{0.4t} - 2.24\sigma_{0.9t} + 0.72\sigma_{1.4t} \tag{16}$$

2.2.2. The FE model of welded joints

The curvature and the weld shape are modelled in a parametric sketch using a Python script. The weld is assumed symmetric, both in x and y direction, with respect to the system origin indicated as 0 in Fig. 6. The symmetry with respect to the y axis is applied through a fully rigid kinematic constraint over the left edge of the model, so that only half of the weld shape is modelled, as in Fig. 7.

The initial curvature of the plate is described by Eq. (1), as for the analytical model. Such distortion applies to the plate field to the right of the weld fusion-line, i.e. the centreline within the weld region (about at least 25 times smaller than the plate field) remains horizontal; see Fig. 7.

A 2D, homogeneous shell section is assigned to the profile, the thickness of which is uniform and equal to the plate width b_p. Thereby, the section described constitutes the middle surface of the 2D FE model. The material is linear-elastic with elastic modulus $E = 207$ GPa and Poisson's ratio $\nu = 0.3$. The model edges are constrained by imposing displacement/rotation boundary conditions at mid-points of the side edges (see Fig. 7), and by defining coupling interactions between the edge surfaces and the mid-points. The coupling interactions are defined so that the edge surface is free to strain over the y-direction. The uniaxial tension is applied as concentrated force P at the mid-point of the right edge, positive in the x-direction. Any out-of-plane deformation is avoided by constraining the related degree of freedom over the whole model. The ABAQUS solver (v6.14−1) performs a static, non-linear geometric analysis of the model using the modified RIKS method with a fixed arc length increment of $1e{-}4$ and a maximum load proportionality factor equal to 1. The 2D model has a structured mesh of 4-noded $S4$ shell elements of thickness b_p in plane-stress condition. This condition imposes zero transverse stress over the thickness of the elements, i.e., over the width of the welded plate. This well represents the behaviour of plate strips. The elements are distributed over the length and thickness directions of the welded plate geometry as in Fig. 8(b). This model corresponds to the blue shaded area depicted in Fig. 8(a), i.e. to the modelled side transversely cut near the weld region by a plane normal to the longitudinal (i.e., X) direction. In Fig. 8(b), the middle surface is highlighted with solid red lines, and it represents the sketch of the 2D model presented in the other figures (see, e.g., Fig. 7).

The mesh is defined in order to capture possible non-linearity in the stress distribution over the model thickness as a consequence of both weld shape and initial distortion. The mesh is uniform and the element size (both in $x-$ and $y-$direction) is 0.2 mm. This means that the mesh has more than 5 elements in length between the constrained edge and the hot-spot location, and 20 elements through the model thickness. Such a fine mesh over the thickness guarantees reliable stresses at the top free surface, where the averaged nodal stresses may depart from the expected linear distribution as a consequence of the numerical

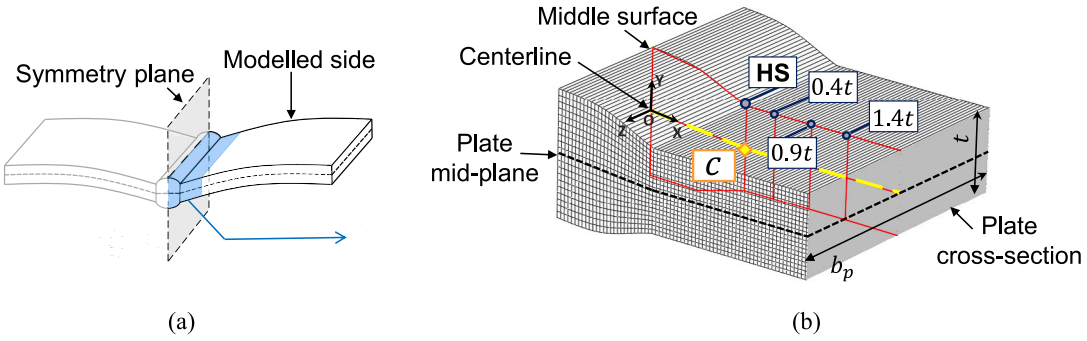

Fig. 8. (a) Schematic representation of the welded plates; (b) view cut of the FE model near the weld region. Geometry parameters and mesh distribution are shown, along with definitions and locations of interest for the present analysis. The origin of the coordinate system is indicated as "o". (For interpretation of the references to colour in this figure legend, the reader is referred to the web version of this article.)

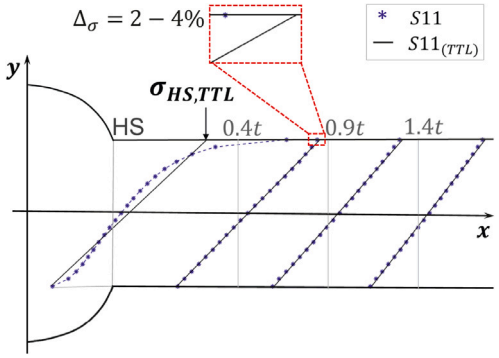

Fig. 9. Post-processing of the normal stress $S11$ by TTL at the weld location HS and at the extrapolation points for the QE approach, i.e. at $x = (0.4, 0.9, 1.4) \cdot t$.

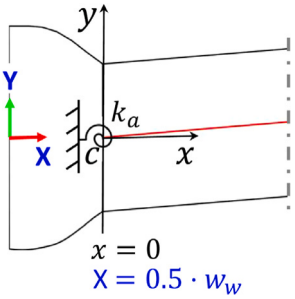

Fig. 10. Geometric equivalence between FE and analytical models, with coordinate systems in capital and italic letters, respectively.

integration scheme. The mesh was selected based on a convergence analysis, where a reference mesh of 0.05 mm-element length and 20 elements over the thickness is considered, along with coarser meshes up to 2 mm-element size. Although the present study uses a very fine mesh, it is noticeable that square elements of size 0.4 or 0.5 mm would be equally good for the concerned model, provided that the mesh remains uniformly distributed. An element aspect ratio of 1 is also preferable for the structural stress extrapolation approach [26]. The convergence analysis is shown in details in Appendix B. With reference to the nomenclature used in Abaqus, the deflection $U2$ in y-direction of the centreline, the slope $UR3|_c$ about the z-axis of the centreline at the weld fusion-line (i.e. at point $c = [x = 0.5w_w, y = 0]$ in Fig. 8), and the normal stress $S11$ in x-direction needed for the TTL and QE approach (see Section 2.2.1) are the results of interest from the FEA. These values are taken at the middle surface shown in Fig. 8. Before the comparison against the analytical model, the stress is linearised through the thickness. For the sake of clarity, this procedure is shown in Fig. 9.

2.3. Fixity factor computation

In this study, the fixity factor is the key parameter that allows the 1D analytical model to consider the weld shape and its effect on plate bending and structural stress. Currently, this parameter cannot be computed analytically. Here, the procedure to compute the fixity factor depends on the FE model response. In particular, on the slope value $UR3|_c$ at point c, which corresponds to the origin of the analytical beam model (i.e. $x = 0$), as shown in Fig. 10. Since the weld region is represented by a rotational spring, the beam length, l, becomes the FE model length, l_{TOT}, reduced by the width of the weld region (i.e., half of the weld width $0.5w_w$).

Based on these definitions, the numerical solution is equalled to the analytical expression of the slope, where ρ_a remains the only unknown.

$$w'|_{x=0} = UR3|_c \tag{17}$$

From the analytical model, w' depends on the term $k = \sqrt{(P/EI_{xx})}$, the BC configuration, and the amplitudes of the initial distortion (y_0 and a_0). The value $UR3|_c$ from the FEA is affected by the weld shape, i.e. by the parameters w_w, h_w, and θ_w. Thereby, the fixity factor can be seen as a function of several parameters, as in Eq. (18).

$$\rho_a = f(w_w, h_w, \theta_w, BCs, k, a_0, y_0) \tag{18}$$

Since it is not possible to define ρ_a analytically, the influence of these parameters is revealed through a sensitivity analysis in Section 5.

3. Case studies for the FE model

In Section 2.3, the weld shape, load level, boundary conditions and initial curvature are indicated as influencing parameters of the fixity factor. About the weld shape, the sensitivity analysis compares three cases of butt-joints in thin plate strips obtained on small-scale thin specimens from literature; see e.g, [27]. The specimens have thickness $t = 4$ mm, length $l_{TOT} = 125$ mm, and width $b_p = 20$ mm. The specifications for each case are summarised in Table 1 (see Fig. 6 as reference) together with the nomenclature to easily refer to the different weld beads later in the manuscript. The abbreviations SB, MB, LB stand for *Small, Medium* and *Large Bead*. These definitions have no general validity, thus being limited to the scope of the present work. A Small Bead corresponds to a small area of the excess weld metal. This area is commonly approximated as $w_w h_w/2$ for both the weld toe and root. In the table, the areas $area_N$ are normalised with respect to the base plate area in the weld region, $w_w t$.

The SB and LB weld shapes are also assessed for different weld widths, while θ_w and h_w are varied for the MB case. All case studies are

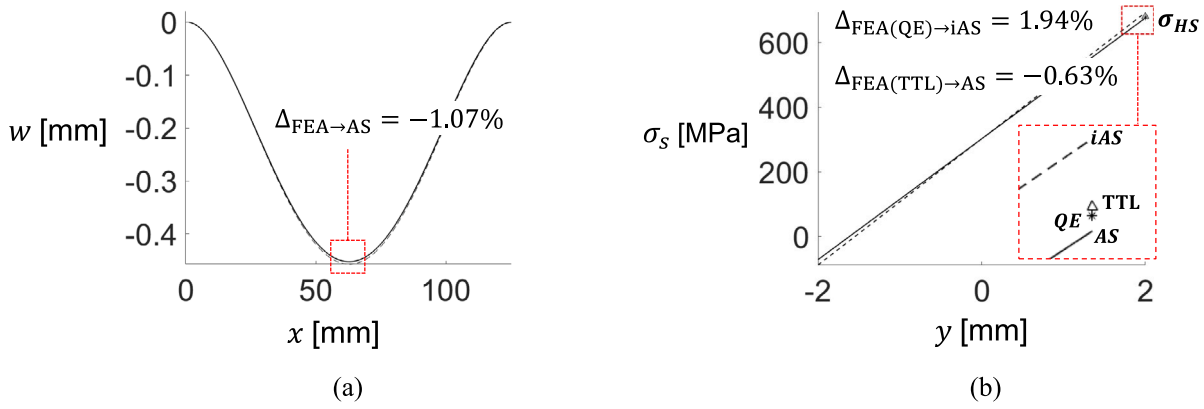

Fig. 11. Comparison between the FE and analytical solutions for (a) deflection w over the beam length and (b) through-thickness structural stress σ_s at weld fusion-line of the fully clamped SB model; $\alpha_l/\alpha_g = 2$ and $\sigma_N = 300$ MPa.

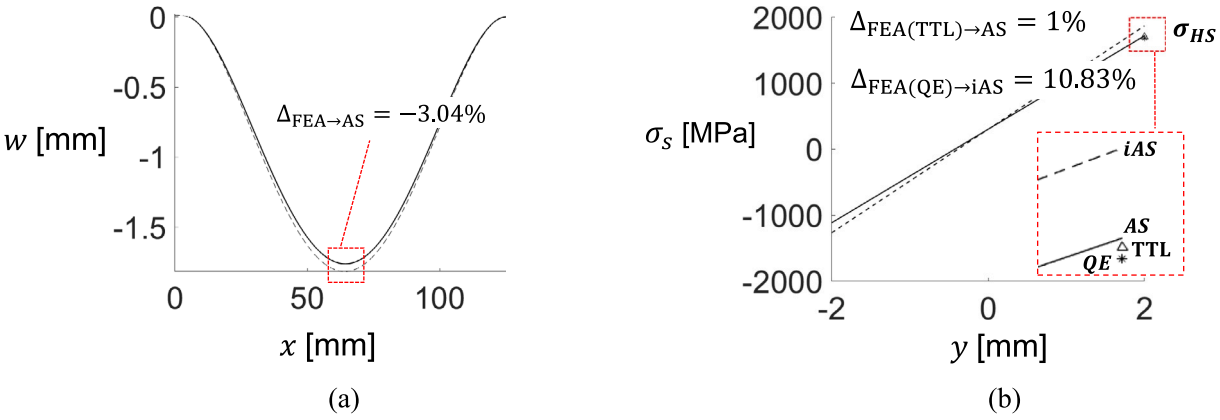

Fig. 12. Comparison between the FE and analytical solutions for (a) deflection w over the beam length and (b) through-thickness structural stress σ_s at weld fusion-line of the fully clamped LB model; $\alpha_l/\alpha_g = 5$ and $\sigma_N = 300$ MPa.

Table 1
Geometric dimensions of the weld bead for three case studies, i.e. *small* (SB), *medium* (MB), and *large* (LB) *weld beads* (see Fig. 6 as reference).

Weld bead	w_w [mm]	h_w [mm]	θ_w [deg]	$area_N$
SB	2.6	0.3	13	0.075
MB	5	0.5	20	0.125
LB	10.6	1.5	30	0.375

simulated for two different amplitudes of the curved distortion, i.e. for $\alpha_l/\alpha_g = [2, 5]$, always being $\alpha_g = 2.5$ deg. Furthermore, the BCs in Fig. 3 are considered. The maximum load level applied in simulations is $\sigma_N = 300$ MPa, which is the highest load experienced in extreme service conditions. This high load is considered given the interest in using high strength steels in the concerned thin-walled structures. The other load levels used in the analysis are 100 MPa, an average standard load range for the given structures, and 200 MPa, as a reference for a high load level in normal service conditions [4]. Although such a broad range is not meaningful in view of low-strength steel applications, it does not prevent the proposed model to be used for these materials, as long as the assumption of elasticity is valid. In fact, as the analysis disregards any nonlinear behaviour of the material, this significant variation of the load is mainly used to point out the sensitivity of the fixity factor computation to such parameter. Notice also that the use of the static RIKS analysis with a fixed arc length increment does not guarantee convergence at the exact applied load. Thereby, the text refers to the load applied to the model, which not necessarily corresponds to the final load level in the simulations. As will be explained in Section 5.1, the analysis of the fixity factor is not sensitive to this fluctuation in the load level.

Finally, Section 6.1 extends the discussion to the variation of the fixity factor in relation to the geometric slenderness l_{TOT}/t of the welded plate. Therefore, data shown in that section refer to a unitary plate width b_p.

4. Validation of the beam model

The comparison between numerical (FEA) and analytical (AS) results is carried in terms of mid-plane deflection (w, where the variable x is omitted) and hot-spot structural stress σ_{HS}. The comparison shows that the procedure to compute the fixity factor allows the 1D beam to well approximate the elastic deformation of a 2D model of the welded plate.

In Fig. 11(a), the deflections are compared for the SB model, i.e. model with a small weld bead. The model has an angle ratio equal to 2, fully clamped BCs and a load of 300 MPa. The consistency between dashed (FEA) and solid (AS) lines is obtained in the hot-spot location, while a difference of approximately 1% is observed for the maximum displacement. The same difference would appear under different BCs. In terms of structural stress, Fig. 11(b) shows that the analytical solution is less than 1% different from the numerical solutions (TTL and QE results indicated by $\triangle$ and $*$, respectively).

The same comparison is shown in Fig. 12 for the LB model, i.e. the model with a large weld bead. The model has angle ratio $\alpha_l/\alpha_g = 5$, BC configuration number 1 in Fig. 3 (i.e., fixed loaded end), and load level of 300 MPa. Overall, this model revealed the largest relative

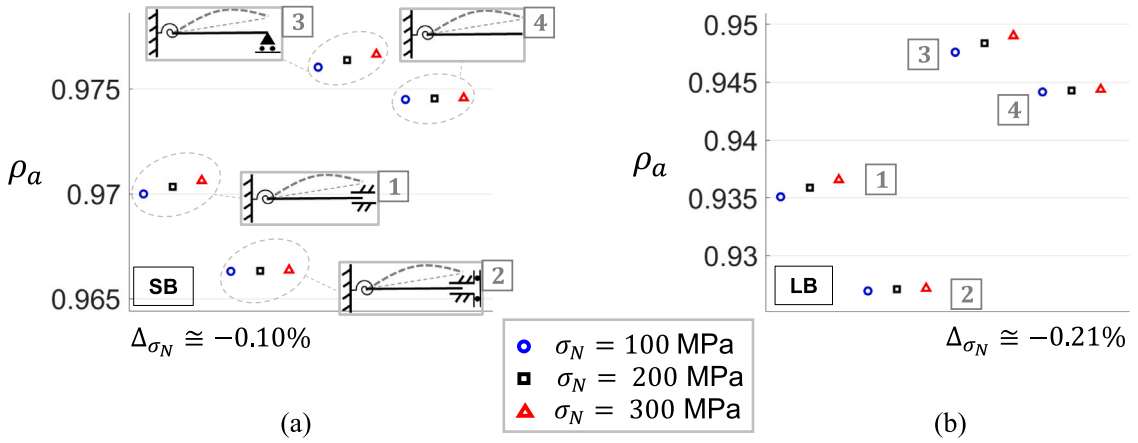

Fig. 13. Fixity factor ρ_a computed under different load levels and BC configurations for (a) SB and (b) LB models. The variation of ρ_a due to the load level is indicated as Δ_{σ_N}.

error in terms of deflections. The analytical model underestimates the maximum displacement from FEA by 3%; see Fig. 12(a). Considering the other BCs, this difference remains approximately 3%. The AS value in the stress comparison is 1% higher than the QE result and is in excellent agreement with the TTL result.

In Figs. 11(b) and 12(b), the maximum relative difference between the two numerical solutions (i.e. TTL and QE) is negligible (around 1%). Moreover, notice that both the figures also show the analytical hot-spot structural stress computed using $\rho_a = 1$, i.e. the ideal analytical solution (iAS). For the SB model, the iAS value has a very good accuracy of approximately 2%. However, for the LB model, the iAS is nearly 11% higher than the extrapolated value. Accordingly, the accuracy of the analytical model improves by up to 9% when the fixity factor is computed.

5. Results of the sensitivity analysis

5.1. Influence of load level and far-end constraint

In case of nonlinear geometry, it is interesting to study the effect of load variation on the rotation, as secondary bending takes place. That is, the moment–rotation curves may anticipate some degrees of nonlinearity as the applied load increases. This could result in a visible variation of the fixity factor ρ_a due to the considered load level. Thereby, in Fig. 13(a) and (b), the fixity factor is computed considering the four different BC configurations and three load levels for the SB and LB model, respectively. The results under the high load level of 300 MPa are shown with red triangles, while black squares and blue circles indicate results under 200 and 100 MPa, respectively. Despite the said nonlinearity, Fig. 13 shows that the load variation only causes a maximum of 0.2% difference in the fixity factor. For this reason, further discussions based on moment–rotation curves are not presented in the context of this study.

About the far-end constraint, the rotational degree of freedom has more influence than the deflection. In percentage, the overall difference between configurations 3 and 2 is around 1% and 2.3% for the SB and LB models, respectively.

The k_m factor for the same models is plotted as a continuous function of the fixity factor in Fig. 14(a) and (b). The plot highlights the difference between the analytical model under analysis and the one with $\rho_a = 1$ (in red triangles). Only the BC configuration number 2 is considered, as it provides the lower values for the fixity factor. It is shown that assuming $\rho_a = 1$ means overestimating the stress by around 3% and 6% for the SB and LB models, respectively.

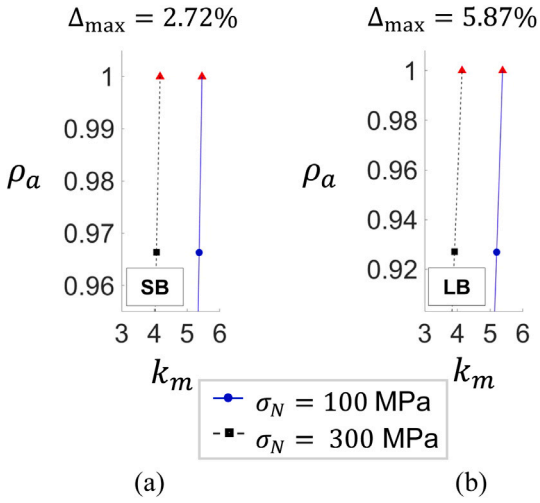

Fig. 14. Stress magnification factor k_m vs. fixity factor ρ_a under different load levels and BC configuration 2 in Fig. 3 for (a) SB and (b) LB models. Δ_{max} is the maximum percentage difference between k_m factors for $\rho_a = 1$ and ρ_a as computed in this study.

5.2. Influence of the initial distortion

The influence of the initial distortion is addressed in Fig. 15. The applied load level is 300 MPa, and all the constraint configurations (from 1 to 4, see Fig. 3) are considered for the LB model. The figure shows that the angle ratio has a relatively small influence on ρ_a. The maximum error reaches $\Delta_{\alpha_l/\alpha_g} = -0.5\%$ for increased angle ratio.

Recalling the results in Fig. 12, the maximum percentage difference between the analytical solutions (i.e., AS and iAS values) is about 9% for an angle ratio equal to 5 and fully clamped BCs, if ρ_a is assumed to be 1.

5.3. Influence of the weld shape

The influence of the weld shape is shown in Fig. 16, where the fixity factors for the SB, MB and LB models are related to the weld normalised areas ($area_N$ in Table 1). The figure also illustrates the different geometries of the weld beads. The results in this section refer to an angle ratio of 2. It is possible to appreciate a relevant change in the fixity factor, which ranges between 0.92 and 1. To understand what is the impact of the single weld parameters, these are varied one-by-one in Sections 5.3.1 and 5.3.2 .

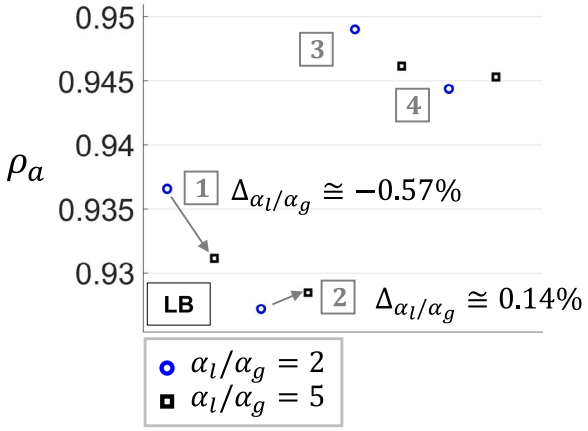

Fig. 15. Fixity factor ρ_a computed for different angle ratios and BC configurations in Fig. 3. The variation of ρ_a due to the angle ratio is indicated as $\Delta_{\alpha_l/\alpha_g}$; the numbers indicate the BC configuration.

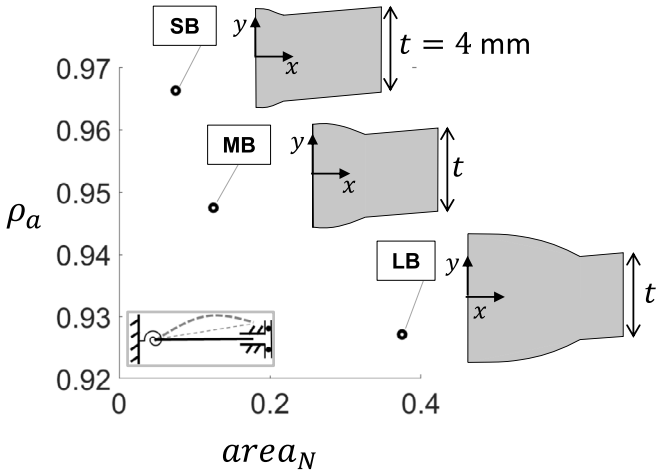

Fig. 16. Comparison between fixity factors ρ_a for different weld normalised areas $area_N$; see Section 3. The BC configuration 2 in Fig. 3 is considered.

5.3.1. Influence of the weld width

Fig. 17(a) and (b) show the influence of the weld width on the fixity factor for the SB and LB models, respectively. According to the results, by doubling the weld width, ρ_a is reduced by around 3%.

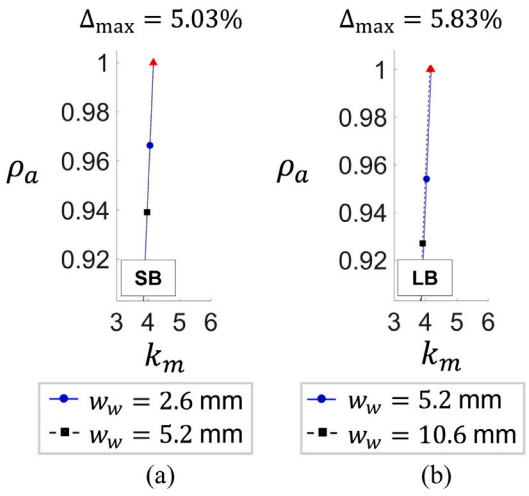

Fig. 18. Stress magnification factor k_m vs. fixity factor ρ_a for different widths of the weld bead and BC configuration 2 in Fig. 3 for (a) SB and (b) LB models. Δ_{max} is the maximum percentage difference between the k_m factor for $\rho_a = 1$ and ρ_a as computed in this study.

Fig. 18 analyses the variation of the k_m factor for different weld widths, including results for $\rho_a = 1$, for the BC configuration 2. A maximum difference of about 5% is shown between the solutions for $\rho_a = 1$ and the ρ_a value computed. Notice that the solid and dashed lines indicating shorter and wider weld, respectively, are almost overlapped. In fact, differently from BCs, load levels, and the angle ratio, weld parameters do not have a direct effect on the k_m factor.

5.3.2. Influence of flank angle and weld reinforcement

The flank angle is responsible for the sharpness of the model transition from the plate cross-section to the weld shape. A larger flank angle results in a sharper transition, i.e., a more severe singularity at the hot-spot location. For a given θ_w, higher weld reinforcement also means a faster transition from the thin plate cross-section to the weld region. It also implies an increment in the flexural stiffness of the model in the weld region. However, the data in Fig. 19 show negligible effects of these parameters on the fixity factor. The figure refers to the MB model (i.e. the model with a medium weld bead dimensions) under an applied load level of 300 MPa. The fixity factor changes by around 0.2% when the angle increases from 10 to 30 deg, see Fig. 19(a), and increases by 0.65% for doubled h_w, see Fig. 19(b). The amplitudes of θ_w and h_w have negligible effect in terms of stress magnification factor.

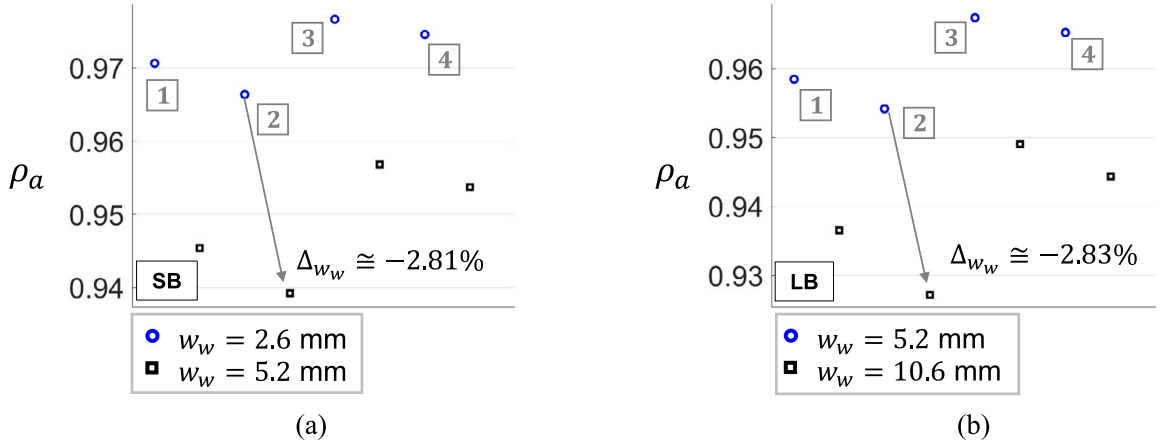

Fig. 17. Fixity factor ρ_a computed for different widths of the weld bead and the BC configurations in Fig. 3 for (a) SB and (b) LB models. The variation of ρ_a due to the weld width is indicated as Δ_{w_w}.

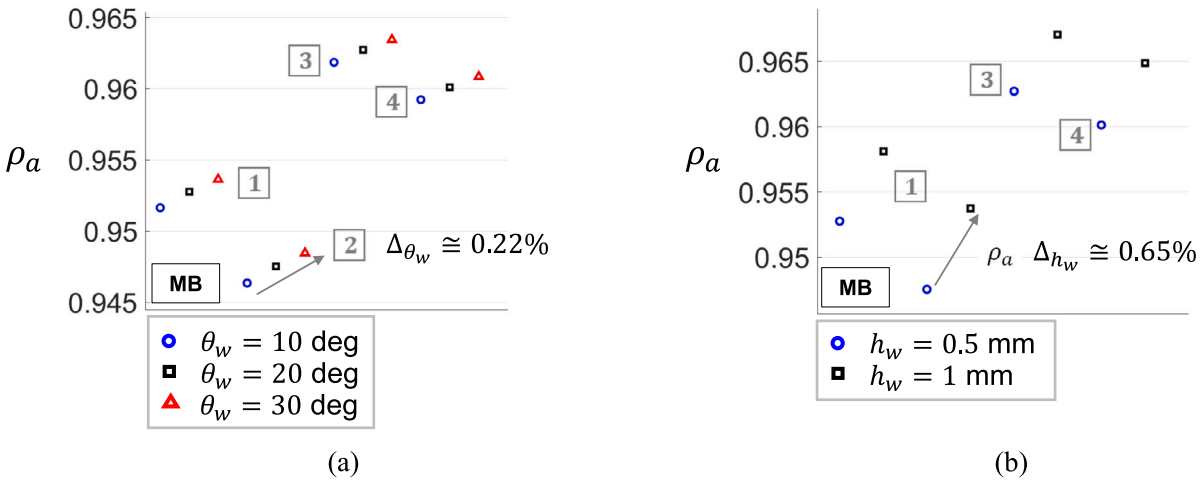

Fig. 19. Fixity factor ρ_a computed for (a) different amplitudes of the weld flank angle and (b) different heights of the weld; numbers indicate the BC configurations in Fig. 3. The variations of ρ_a due to the flank angle and the height of the weld are indicated as Δ_{θ_w} and Δ_{h_w}, respectively.

6. Discussion

The analysis in Section 5 resulted in ρ_a values higher than 0.92 (see, e.g., Fig. 15). According to the classification in the Eurocode 3 for the design of steel structures [20,28], a connection in an unbraced frame is assumed as ideally rigid when the ratio between the rotational stiffness of the connection and the beam stiffness (EI_{xx}/l) is at least 25, i.e. when $\rho_a \geq 0.87$ (and even smaller for braced frames). In the stability analysis of frames, this assumption has trivial effects on the displacement field. However, a negligible error on the deflection leads to higher inaccuracy of the results in terms of hot-spot structural stress. In fact, as shown in Section 5, considering an ideally rigid BC at the weld location results in nearly 9% error in the stress magnification factor k_m. On one hand, the assumption of ideal BC (i.e. $\rho_a = 1$) affects the structural stress computation in a conservative way, thus remaining a safe option. On the other hand, a 9% overestimation in k_m leads to an underestimation in terms of fatigue life. The error reaches about 54% for an S–N curve with slope $m = 5$, which is recommended for thin and flexible welded plates [29]. This would mislead on the reliability of the structures and hinder the development of lightweight solutions. Thereby, this discussion disregards the assumption of ideally rigid connection suggested by the classification for joints with $\rho_a \geq 0.87$.

Given that the observed results are limited to the three case studies described in Table 1, it is interesting to observe the trend of the fixity factor as a function of the slope of the mid-plane at the weld fusion-line (i.e., $UR3|_c$, where $c = [0.5 \cdot w_w, 0]$ is shown in Fig. 8(b)), so as to have a general understanding that goes beyond the characteristics of the weld beads. In Fig. 20, the fixity factors of the SB and LB models are shown with circles on solid lines and squares on dashed lines, respectively, for BC configuration 1 (in blue) and 2 (in black). The applied load level is 100 MPa. When the fixity factor is plotted as a function of the slope at the hot-spot location, the main role is played by the BC at the loaded end rather than by the shape of the weld bead. However, it is possible to observe that the SB model results in a more rigid rotational constraint, in consistency with Fig. 16. This happens because the hot-spot location is closer to the rigid left-edge of the model, due to narrower weld and narrower deforming zone in the 2D-FE model. This explains a smaller slope value at the hot-spot of the SB model, despite the weld of the LB model has a higher stiffness provided by a larger weld reinforcement. This confirms that the weld width w_w has a major impact on the fixity factor variation. A different BC configuration at the far-end determines a different trend for the fixity factor in relation to the slope. Although the blue and black lines all converge to $\rho_a = 1$ when the slope is 0, the blue lines (related to the BC configuration 2) tend to $\rho_a = 0$ faster than the others when the slope magnitude increases. As a result of the different convergence rates, the blue lines also show a non-linear trend, while the black lines remain visually linear. As a physical explanation, the fully fixed boundary condition implies a higher moment reaction,

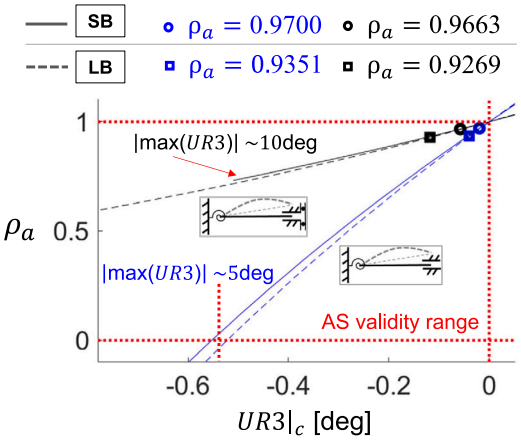

Fig. 20. Slope $UR3|_c$ vs. fixity factor ρ_a at a load level of 100 MPa for SB and LB models with BC configurations 1 and 2. (For interpretation of the references to colour in this figure legend, the reader is referred to the web version of this article.)

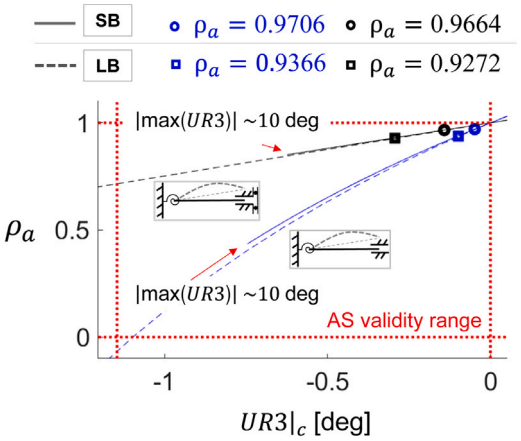

Fig. 21. Slope $UR3|_c$ vs. fixity factor ρ_a at a load level of 300 MPa for SB and LB models with BC configurations 1 and 2. (For interpretation of the references to colour in this figure legend, the reader is referred to the web version of this article.)

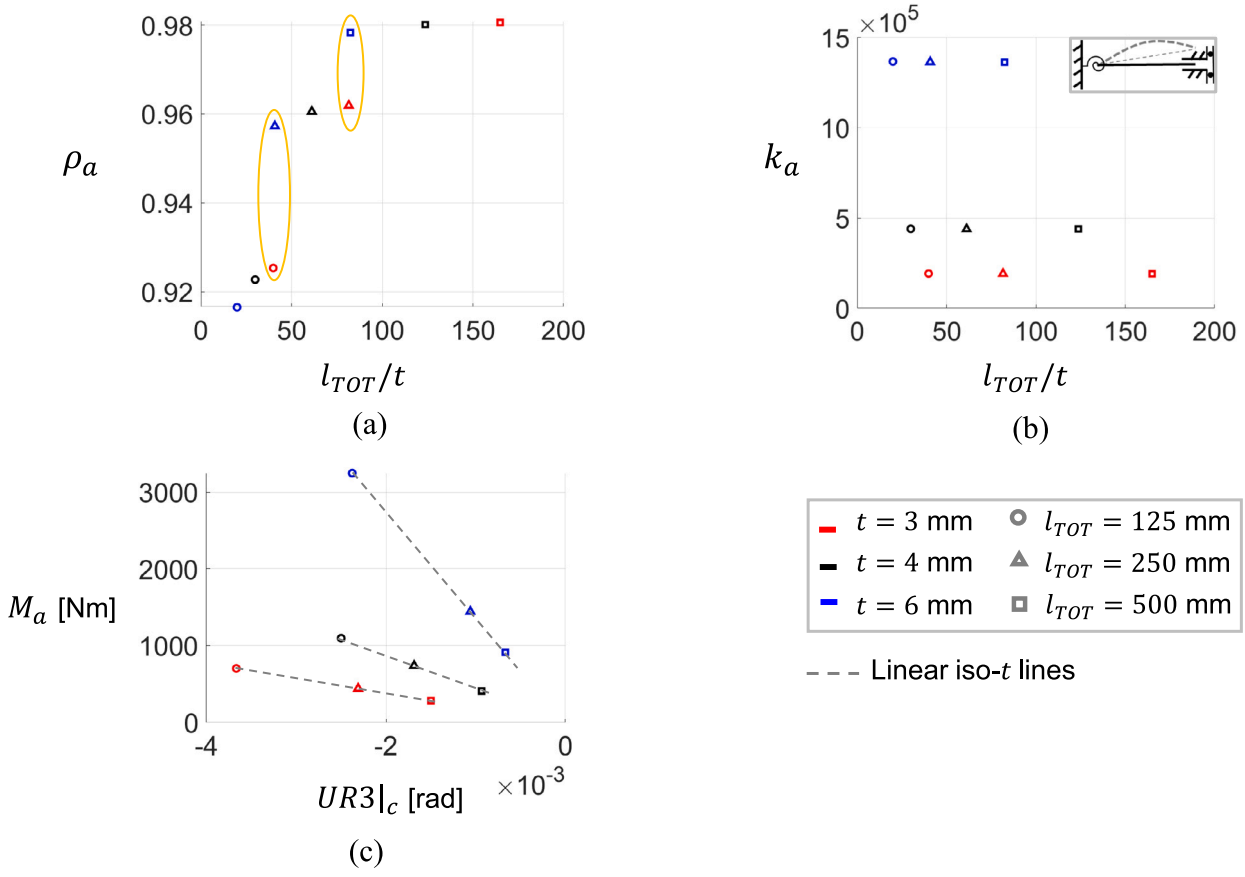

Fig. 22. Influence of the slenderness ratio l_{TOT}/t on (a) fixity factor ρ_a and (b) spring rotational stiffness k_a; (c) moment–slope relationship (M_a vs. $UR3|_c$). BC configuration 2 in Fig. 3 and $\sigma_N = 100$ MPa are considered.

which is due to the contribution from the shear force preventing the vertical deflection at the far-end. Thereby, the actual slope is reduced, thus resulting in a higher fixity factor, at same load level and for the same weld shape. This also means that, at the same given conditions, a fully fixed beam would reach the same slope of a beam free to deflect only in the case of lower rotational stiffness of the weld region (i.e. lower fixity factor). In addition, the slope range shown in the figure is so that the maximum allowed rotation over the whole beam length reaches 10 deg, which is considered a threshold for the validity of the von-Kármán kinematic assumption of moderate rotations. Thus, the straight dashed red lines in the figure indicate the validity range of the analytical solution (AS) presented in this paper.

In Fig. 21, the same functions are plotted for an applied load level of 300 MPa. In this case, the blue lines reach a zero fixity factor when the maximum slope over the beam length is around 5 deg (see dashed red lines).

Notice that the validity ranges indicated by the dashed red lines in both the figures are far from affecting the use of the present analytical model for the considered structural problem. According to the given validity limits, the semi-analytical computation of the fixity factor is generally reliable as long as the global behaviour of the structure remains elastic. Thereby, in applying the proposed procedure, it is advised to check that any effect due to the singularity remains local, i.e., the mid-plane of the plate undergoes small displacements and moderate rotations (as for the von-Kármán assumption). This is a more general approach than considering the elastic range in terms of load limits, as it does not depend on additional factors (e.g., in-plane stress redistribution, imperfections) that may alter the load analysis.

6.1. Generalisation of the results

To understand the general validity of the results in Section 5, the impact of the plate geometric slenderness, l_{TOT}/t, on the fixity factor is now discussed. Fig. 22(a) and (b) show the fixity factor ρ_a and the corresponding rotational stiffness k_a for increasing l_{TOT}/t, respectively. The model considered for this analysis has unitary plate width b_p. The weld width is kept constant and equal to $w_w = 10.6$ mm, while the flank angle and the weld height are adapted to the thickness variation, i.e. $h_w = 0.75 \cdot t/2$ and $\theta_w = \arctan[h_w/(w_w/2)]$, respectively. The angle ratio is equal to 2 and the load applied is 100 MPa. The plot refers to the BC configuration number 2 in Fig. 3, which gives the lowest fixity factors overall. The slenderness ratio varies both in thickness and length. From the lowest (~21) to the highest (~166) ratio, the fixity factor increases by 7%, which is mainly due to the variation of the beam length. At given length, the increase of t is responsible for less than 1% decrease in ρ_a. On the contrary, k_a decreases by an order of magnitude with a decrease in the beam thickness, while the increase in the beam length only causes a 0.4% decrease in stiffness. This is also explained by Eq. (11), where the parameter k_a is proportional to t^3/l. It is observed that for the same ratio but different values of l_{TOT} and t, the results are different (see values in yellow circles). This suggests that at a fixed slenderness ratio, larger dimensions of the plate results in a more rigid solution.

In Fig. 22(c), the moment–slope relationship (M_a vs. $UR3|_c$) at the welded end of the beam is shown. The figure also indicates trend lines at constant thickness and varying length (i.e., iso-t lines in dashed grey). While these lines show a linear trend, the proportionality between the moment–slope relationship and t is of a higher order. This reflects the beam elementary mechanics, for which the slope of a simply supported beam subjected to end moments is defined as in

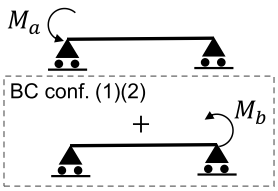

$$\Phi_a = \frac{M_a l}{3EI_{xx}} - \frac{M_b l}{6EI_{xx}}, \quad \text{where} \quad I_{xx} \propto t^3$$

Fig. 23. Moment–slope relation based on elementary beam mechanics.

Fig. 23 [20,21]. Notice that Fig. 22(c) does not show a clear third-order proportionality with t due to slightly different load levels in the RIKS analysis of the models.

Based on Fig. 22, an increased slenderness ratio means a higher fixity factor, despite the moderate increase in slope for shorter beams. This means that the weld has a minor effect on the bending behaviour of components with higher slenderness ratios. In response, the term k_a can be seen as a modified flexural stiffness of the beam. Accordingly, in the case under analysis, k_a mainly depends on the beam geometric characteristics (i.e., by I_{xx}/l) rather than the spring. Thereby, the assumption of non-ideal BC at the weld location becomes less relevant for increased geometric slenderness ratio. This extends the validity of this study to the treatment of thin and slender plate strips. In fact, the inaccuracy of the analytical model in evaluating the mechanics of thin and slender plates would remain under the 3% showed in Section 4.

7. Conclusion

The present study investigated an analytical beam model for the analysis of thin plate butt-welded joints with an initial curved distortion. A rotational spring allowed the 1D beam model to account for the rotational rigidity of the butt-joint in terms of a fixity factor ρ_a. The study proposed a semi-analytical method to compute the fixity factor of the spring for the beam under uniaxial tension load. The validity of the method is based on the assumption of small displacement and moderate rotation of the mid-plane of the welded plate.

The beam model was validated with a maximum inaccuracy of 3% against a 2D FE model of the welded plate. The consistency between the analytical and numerical models suggests that the difference between the 2D model and the analytical solution for ideal BCs (i.e., $\rho_a = 1$) is mainly due to the rotational rigidity at plate supports, rather than additional phenomena such as in-plane shear effects. As the present study focused on thin and slender plate strips, large-scale structures with transverse normal and shear stresses would need further investigations. Furthermore, these future developments could consider an extensive analysis on the variation of the proportional limit for the concerned connection in order to understand the effect of stress redistribution due to local plasticity under high loading conditions. Finally, the validation of the beam analytical model for a 2D FE model is still limited to simplified curved initial distortions of plates and to the assumption of fully symmetric shapes of the weld bead.

According to a sensitivity analysis, ρ_a is mainly affected by the weld width and the far-end constraint. Overall, data resulted in ρ_a values between 0.92 and 1. The corresponding variation in terms of stress magnification factor k_m showed generally small differences. However, assuming $\rho_a = 1$ may lead to a stress overestimation up to around 9% with respect to the analytical model with the non-ideal constraint. This means a conservative underestimation in terms of fatigue life of components (up to nearly 54%, for $m = 5$). Although these numbers suggest the need of retaining the fixity factor in the analytical solution, it is noticeable that considering $\rho_a = 1$ at the welded end provides only slightly conservative, thus reliable, estimation of the k_m factor for high slenderness ratios.

CRediT authorship contribution statement

Federica Mancini: Conceptualization, Methodology, Investigation, Resources, Software, Validation, Visualization, Writing – original draft. **Heikki Remes:** Conceptualization, Methodology, Supervision, Investigation, Resources, Writing – review & editing. **Jani Romanoff:** Conceptualization, Methodology, Investigation, Resources, Writing – review & editing. **Pasquale Gallo:** Resources, Writing – review & editing.

Declaration of competing interest

The authors declare that they have no known competing financial interests or personal relationships that could have appeared to influence the work reported in this paper.

Acknowledgements

The research presented in this paper is related to the European Commission funded Horizon 2020 project entitled “Realisation and Demonstration of Advanced Material Solutions for Sustainable and Efficient Ships” (RAMSSES).

Appendix A. Stress magnification factor formulations

A.1. Formulations for $\rho_a = 1$

When ideal BC is assumed at the weld location, i.e. $\rho_a = 1$, the stress magnification factor for welded plates with local angular misalignment can be computed as in Eqs. (A.1), (A.2), (A.3), and (A.4) [15]. In the equations, $\beta = (2l/t)\sqrt{3\sigma_m/E}$, where σ_m is the tensile membrane stress applied to the structure. Notice that $k_{m,x}$ indicates the k_m factor considering the BC configuration number x in Fig. 3.

$$k_{m,1} = 1 + \frac{6a_0\pi}{t}\frac{\beta}{(\pi^2+\beta^2)\tanh\left(\frac{\beta}{2}\right)} \tag{A.1}$$

$$k_{m,2} = 1 + \frac{3y_0}{t}\frac{\tanh\left(\frac{\beta}{2}\right)}{\frac{\beta}{2}} + \frac{6a_0\pi}{t}\frac{\beta}{(\pi^2+\beta^2)\tanh\left(\frac{\beta}{2}\right)} \tag{A.2}$$

$$k_{m,3} = 1 + \frac{6a_0}{t}\frac{\pi\beta\tanh(\beta)}{(\pi^2+\beta^2)} \tag{A.3}$$

$$k_{m,4} = 1 + \frac{6y_0}{t}\frac{\tanh(\beta)}{\beta} + \frac{6a_0}{t}\frac{\pi\beta\tanh(\beta)}{(\pi^2+\beta^2)} \tag{A.4}$$

A.2. Formulations for $\rho_a \neq 1$

As a non-ideal rotational constraint at the weld location is considered, the equations depend on the unknown parameter ρ_a. The formulations for the stress magnification factor are provided as a Matlab script. Below, `k_mx` indicates the k_m factor considering the BC configuration number `x` in Fig. 3.

```
S_n=; %Applied nominal stress [Pa], S_n > 0 for tensile stress
E=; %Young's modulus  [Pa]
l=; %beam length  [m]
t=; %beam thickness     [m]
angle_ratio=;
alpha_g=; %global angle $\alpha_g$  [deg]
alpha_l=angle_ratio*alpha_g; %local angle $\alpha_l$
y_0=(tan(alpha_g)*l);
a_0=((tan(alpha_l-alpha_g))*l/pi);
beta=(2*l/t)*sqrt(3*S_n/E);
rho_a=;%fixity factor
```

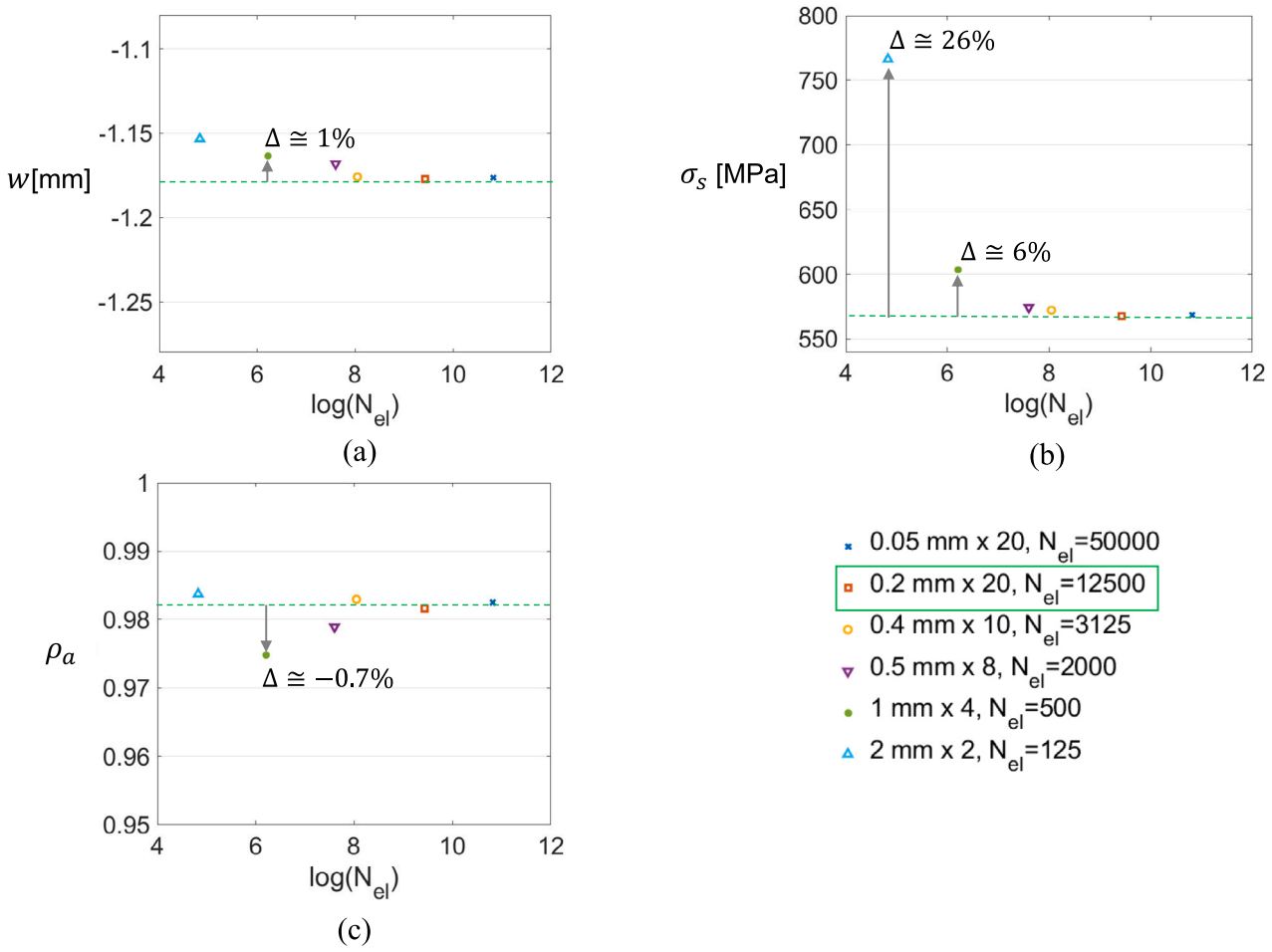

Fig. B.24. (a) Deflections w, (b) structural stress σ_N, and (c) fixity factor ρ_a as a function of the total number of elements used (in log scale), for the BC configuration 1; the final mesh selected for the current study is highlighted by a green box. (For interpretation of the references to colour in this figure legend, the reader is referred to the web version of this article.)

```
%BC configuration 1
k_m1_num=24*a_0*rho_a*beta*pi*(cosh(beta)*beta+beta-2*sinh(beta));
k_m1_den=-t*(beta^2+pi^2)*(((-1+rho_a)*beta^2+8*rho_a)*cosh(beta)...
+(-5*rho_a+1)*beta*sinh(beta)-8*rho_a);
k_m1=1+k_m1_num/k_m1_den

%BC configuration 2
k_m2_num=24*(((-a_0*pi-y_0)*beta^2-pi^2*y_0)*cosh(beta)...
+(-a_0*pi+y_0)*beta^2+pi^2*y_0)*rho_a;
k_m2_den=-t*(-beta^2*(-1+rho_a)*cosh(beta)+beta*4*rho_a*sinh(beta))...
*(pi^2+beta^2);
k_m2=1+k_m2_num/k_m2_den

%BC configuration 3
k_m3_num=-18*sinh(beta)*pi*a_0*beta^2*rho_a;
k_m3_den=-(pi^2+beta^2)*t*(((+1-rho_a)*beta^2-3*rho_a)*sinh(beta)...
+3*cosh(beta)*beta*rho_a);
k_m3=1+k_m3_num/k_m3_den

%BC configuration 4
k_m4_num=18*rho_a*sinh(beta)*((-a_0*pi-y_0)*beta^2-pi^2*y_0);
k_m4_den=-(pi^2+beta^2)*t*(-beta*(-1+rho_a)*sinh(beta)...
+3*cosh(beta)*rho_a)*beta;
k_m4=1+k_m4_num/k_m4_den
```

Appendix B. Convergence analysis

The results of the convergence analysis are shown for BC 1 in Fig. B.24. The selected mesh (0.2 mm × 20 el.s through the thickness, i.e. 12 500 elements in total) is indicated by a green box. Fig. B.24(a), (b) and (c) show that coarser meshes of 0.4 and 0.5 mm would be equally reliable in terms of deflections, structural stress, and fixity factor, respectively. Although the results for deflections and fixity factors seemed to be rather independent on the element size, a clear convergence curve can be observed for the stress in Fig. B.24. Above 1 mm-element mesh, the stress error overcomes the 6% and increases up to 26% for the coarsest mesh. When the selected mesh (0.2 mm-element mesh) is compared to a finer mesh with $S4$ elements of 0.05 mm length, and 0.2 mm height (i.e., 20 elements through the thickness), deflections, stresses and fixity factors only differ by less than 0.1%. The same is true for different BC configurations.

References

[1] Herrmann C, Dewulf W, Hauschild M, Kaluza A, Kara S, Skerlosa S. Life cycle engineering of lightweight structures. CIRP Ann 2018;67(2). http://dx.doi.org/10.1016/j.cirp.2018.05.008, 651-67a.

[2] Romanoff J, Remes H, Varsta P, Goncalves BReinaldo, Körgesaar M, Lillemäe-Avi I, et al. Limit state analyses in design of thin-walled marine structures - some aspects on length-scales. J Offshore Mech Artic Eng ASME 2018;11B(3). http://dx.doi.org/10.1115/OMAE2018-78304.

[3] Remes H, Romanoff J, Lillemäe I, Frank D, Liinalampi S, Lehto P, Varsta P. Factors affecting the fatigue strength of thin-plates in large structures. Int

J Fatigue 2017;101:397–407. http://dx.doi.org/10.1016/j.ijfatigue.2016.11.019, Elsevier.
[4] Lillemäe I, Remes H, Romanoff J. Influence of initial distortion on the structural stress in 3mm thick stiffened panels. Thin-Walled Struct 2013;72:121–7. http://dx.doi.org/10.1016/j.tws.2013.07.001.
[5] Lillemäe-Avi I, Remes H, Dong Y, Garbatov Y, Quemener Y, Eggert L, et al. Benchmark study on considering welding-induced distortion in structural stress analysis of thin-plate structures. 2019, p. 387–94. http://dx.doi.org/10.1201/9781315157368-45, 9781138069077.
[6] Niemi E, Fricke W, Maddox SJ. Structural hot-spot stress approach to fatigue analysis of welded components. In: IIW Collection, Vol. 13. Springer; 2018, p. XIII, 76. http://dx.doi.org/10.1007/978-981-10-5568-3.
[7] Hobbacher AF. Recommendations for fatigue design of welded joints and components. Springer; 2016, p. 47. http://dx.doi.org/10.1007/978-3-319-23757-2.
[8] Kuriyama Y, Saiga Y, Kamiyama T, Ohno T. Low cycle fatigue strength of butt welded joints with angular distortion. Iiw doc x111-621-71, 1971.
[9] Lillemäe I, Liinalampi S, Remes H, Itävuo A, Niemelä A. Fatigue strength of thin laser-hybrid welded full-scale deck structure. Int J Fatigue 2017;95:282–92. http://dx.doi.org/10.1016/j.ijfatigue.2016.11.012, Elsevier.
[10] Det Norske Veritas AS. Fatigue assessment of ship structures. DNV Classif Notes 2014;30(7). https://rules.dnvgl.com/docs/pdf/DNVGL/CG/2015-10/DNVGL-CG-0129.pdf.
[11] Zhou W, Dong P, Lillemäe I, Remes H. A 2nd- order SCF solution for modeling distortion effects on fatigue of lightweight structures. Weld World 2019;63(6):1695–705. http://dx.doi.org/10.1007/s40194-019-00772-7, Springer.
[12] Dong P, Zhou W, Xing S. An analytical method for interpreting distortion effects on fatigue test results of thin plate panel specimens. Weld World 2019;63(6):1707–14. http://dx.doi.org/10.1007/s40194-019-00791-4, Springer.
[13] Shen W, Qiu Y, Li C, Hu Y, Li M. Fatigue strength evaluation of thin plate butt joints considering initial deformation. Int J Fatigue 2019;125:85–96. http://dx.doi.org/10.1016/j.ijfatigue.2019.03.036, Elsevier.
[14] Shen W, Qiu Y, Xu L, Song L. Stress concentration effect of thin plate joints considering welding defects. Ocean Eng 2019;184:273–88. http://dx.doi.org/10.1016/j.oceaneng.2019.05.019, Elsevier.
[15] Mancini F, Remes H, Romanoff J, Goncalves BReinaldo. Stress magnification factor for angular misalignment between plates with welding-induced curvature. Weld World 2020;64(4):729–51. http://dx.doi.org/10.1007/s40194-020-00866-7, Springer.
[16] Mancini F, Remes H, Romanoff J. A stress magnification factor for plates with welding-induced curvatures. Int Conf Offshore Mech Arct Eng ASME 2020;84324:V02AT02A031. http://dx.doi.org/10.1115/OMAE2020-18094.
[17] Bazant ZP, Cedolin L, Hutchinson JW. Stability of structures: elastic, inelastic, fracture, and damage theories. World Scientific; 2010, http://dx.doi.org/10.1142/7828.
[18] Ventsel E, Krauthammer T, Carrera E. Thin plates and shells: theory, analysis, and applications. Appl Mech Rev 2002;55(4):B72–3. http://dx.doi.org/10.1115/1.1483356.
[19] Monforton GR, Wu TS. Matrix analysis of semi-rigidly connected frames. J Struct Div Amer Soc Civ Eng 1963;89(6):13–42. http://dx.doi.org/10.1061/JSDEAG.0000997.
[20] Chen WF, Lui EM. Handbook of structural engineering. CRC Press; 2005, 9780849315695.
[21] Hellesl J. Mechanics and effective lengths of columns with positive and negative end restraints. Eng Struct 2007;29(12):3464–74. http://dx.doi.org/10.1016/j.engstruct.2007.08.021, Elsevier.
[22] Reddy JN. An introduction to nonlinear finite element analysis: with applications to heat transfer, fluid mechanics, and solid mechanics. OUP Oxford; 2015, http://dx.doi.org/10.1093/acprof:oso/9780199641758.001.0001, http://dx.doi.org/10.1007/s40194-016-0326-8.
[23] Remes H, Fricke W. Influencing factors on fatigue strength of welded thin plates based on structural stress assessment. Weld World 2014;58(6):915–23. http://dx.doi.org/10.1007/s40194-014-0170-7, Springer.
[24] Dong P. A structural stress definition and numerical implementation for fatigue analysis of welded joints. Int J Fatigue 2001;23(10):865–76. http://dx.doi.org/10.1016/S0142-1123(01)00055-X, Elsevier.
[25] Doerk O, Fricke W, Weissenborn C. Comparison of different calculation methods for structural stresses at welded joints. Int J Fatigue 2003;25(5):359–69. http://dx.doi.org/10.1016/S0142-1123(02)00167-6, Elsevier.
[26] Poutiainen I, Tanskanen P, Marquis G. Finite element methods for structural hot spot stress determination—a comparison of procedures. Int J Fatigue 2004;26(11):1147–57. http://dx.doi.org/10.1016/j.ijfatigue.2004.04.003, Elsevier.
[27] Lillemäe I, Remes H, Liinalampi S, Itävuo A. Influence of weld quality on the fatigue strength of thin normal and high strength steel butt joints. Weld World 2016;60(4):731–40, Springer.
[28] Silva LSDa, Simões R, Gervásio H. Design of steel structures: eurocode 3: design of steel structures, part 1-1: general rules and rules for buildings. John Wiley & Sons; 2012.
[29] Sonsino CM, Bruder T, Baumgartner J. SN lines for welded thin joints — suggested slopes and FAT values for applying the notch stress concept with various reference radii. Weld World 2010;54(11):R375–92. http://dx.doi.org/10.1007/BF03266752, Springer.